Classification of skyrmionic textures and extraction of Hamiltonian parameters via machine learning

Dushuo Feng,[1] Zhihao Guan,[1] Xiaoping Wu,[1] Yan Wu◉,[1] and Changsheng Song◉[1,2,*]

[1]*Key Laboratory of Optical Field Manipulation of Zhejiang Province, Department of Physics, Zhejiang Sci-Tech University, Hangzhou 310018, China*
[2]*Longgang Institute of Zhejiang Sci-Tech University, Wenzhou 325802, China*

Classifying skyrmionic textures and extracting magnetic Hamiltonian parameters represent crucial and challenging pursuits within the realm of two-dimensional (2D) spintronics. In this study, we leverage micromagnetic simulation and machine learning (ML) to theoretically achieve the recognition of nine distinct skyrmionic textures and the extraction of magnetic Hamiltonian parameters from extensive spin texture images in a 2D Heisenberg model. For texture classification, a deep neural network (DNN) trained through transfer learning is proposed to enable the accurate discrimination of nine diverse skyrmionic textures. In parallel, for parameter extraction, based on the textures generated by different Heisenberg exchange stiffnesses (J), Dzyaloshinskii-Moriya strengths (D), and anisotropy constants (K), we employ a multi-input single-output (MISO) deep learning model (handling both images and parameters) and a support vector regression (SVR) model (dealing with Fourier features) to extract the parameters embedded in the spin textures. Our models for classification and extraction demonstrate significant success, achieving an accuracy of 98% (DNN), and R-squared (R^2) of 0.90 (MISO) and 0.8 (SVR). Notably, our ML methods prove their effectiveness in distinguishing skyrmionic textures with blurred phase boundaries, thereby contributing to a more nuanced understanding of these textures. Additionally, our models establish a mapping relationship between spin texture images and magnetic parameters, thus validating the feasibility of extracting microscopic mechanisms from experimental images. This finding offers significant guidance for spintronics experiments, emphasizing the potential of ML methods in elucidating intricate details from practical observations.

I. INTRODUCTION

Various spin textures observed from two-dimensional (2D) magnets [1,2], representing distinct phases, arise from the competition between magnetic anisotropy and short-range exchange, such as Heisenberg exchange and Dzyaloshinskii-Moriya interaction (DMI) [3–7]. Across various magnetic systems, both theoretical studies and experimental investigations have explored the morphology and stability of intricate magnetic domain configurations, including stripes, labyrinths, chevrons, and bubbles [8–10]. Simultaneously, extensive efforts have been directed toward understanding the phase transitions involving chiral magnetic textures such as spin helices or chiral domain walls, notable for their extended lifetimes [11].

Recently, there has been a heightened focus on topological chiral magnetic spin textures, including skyrmions [12–14], merons [15,16], and other toroidal topological states [17,18]. These have garnered attention for their promising applications in future spintronic devices, offering high storage density and energy efficiency [19,20] due to their distinctive static and dynamic properties. Moreover, the detection of skyrmions in various magnetic materials, such as MnGe [21], FeGe [22], CrTe$_2$ [23], CrISe [24], and 2D Janus materials [25], highlights the significance of the asymmetric DMI [26,27] in generating and stabilizing these intriguing topological chiral textures. Despite the well-established knowledge of spin configurations in magnetic systems, the understanding of topological spin textures, encompassing spin chirality and intricate interactions, remains incomplete.

Quantifying the properties of 2D magnets often relies on specific magnetic parameters. Extracting these parameters appropriately allows for a theoretical understanding and prediction of the system's characteristics [28]. For example, the micromagnetic model can evolve the spin configurations to the stable state based solely on the magnetic Hamiltonian [29]. The typical magnetic Hamiltonian comprises several terms. Specifically, Heisenberg

exchange energy attempts to align neighboring spins; DMI favors the tilting of neighboring spins; and the purpose of magnetocrystalline anisotropy energy is to align the spins with the anisotropy direction or perpendicular to the anisotropy axis [30]. These terms are determined by parameters such as Heisenberg exchange stiffness (J), Dzyaloshinskii-Moriya strength (D), and anisotropy constant (K), respectively [31].

Prior research has dedicated substantial efforts to extracting key parameters from magnets using methods like neutron scattering [32,33], Brillouin light scattering, or ferromagnetic resonance [34–37]. However, these approaches are time-consuming and costly because of the reliance on the inevitable measurements of time-resolved dynamics [30,38,39]. Furthermore, with the latest development of Lorentz transmission electron microscopy and other magnetic observing technologies, experimental images can provide more detailed information of spin configurations. While spin configurations are determined by the magnetic Hamiltonian, extracting precise Hamiltonian parameter values solely from images within the vast Hilbert space [40] poses a challenging task. Consequently, there is a pressing need for the automatic and efficient extraction of Hamiltonian parameters from experimental or simulated images.

Machine learning algorithms possess remarkable capabilities for learning from labeled data and effectively handling extensive datasets. They offer an efficient approach to studying diverse physical phenomena in condensed matter physics, spanning from representing quantum states [41] to the discovery of phase transitions [42–44] and the recognition of conventional phases of matter [45]. On the one hand, convolutional neural networks (CNNs) have been successfully applied to the following tasks: identifying the phases [46,47], detecting the phases from videos of spin lattices [48], and constructing low-temperature phase diagrams for models that includes anisotropy terms [49]. Additionally, CNNs have demonstrated effectiveness in predicting magnetic features such as chirality [50], the topological charge [51], and the DMI [52] from 2D images of spin configurations. However, many of the previous studies in this field concentrate on characterizing typical configurations, overlooking the intermediate and indistinguishable phases emerging from thermal fluctuations [53], Notably, there is a scarcity of works focusing on the prediction of magnetic Hamiltonian parameters combined with spin texture recognition.

This study delves into the classification of skyrmionic textures and the extraction of magnetic Hamiltonian parameters within the 2D Heisenberg model, incorporating Heisenberg exchange interaction (J), Dzyaloshinskii-Moriya interaction (D), and single-ion anisotropy (K) through a combination of machine learning (ML) and micromagnetic simulation (MS). We produce the datasets of 6000 spin textures encompassing nine different phases

obtained from MS. For phase classification, we propose an automated labeling framework employing unsupervised ML algorithms such as K-means and hierarchical clustering to categorize the original images into different spin phases. Leveraging the Detection Transformer (DETR) algorithm, we achieve accurate skyrmion recognition and analyze the impact of magnetic field and temperature on magnetic phase transitions. A standard deep neural network (DNN) trained from transfer learning is applied efficiently for distinguishing phase boundaries among the topologically protected magnetic skyrmion states, spin spirals originating from the spin-orbit coupling, and other mixed states with a high accuracy of 98%.

Subsequently, we construct precise accurate phase diagrams under the manipulation of temperature, magnetic field, and magnetic Hamiltonian parameters J, D, and K, achieving remarkable agreement when compared with simulation results. Furthermore, we devise a multi-input single-output (MISO) deep learning model for the extraction of magnetic Hamiltonian parameters which reaches a high R-squared (R^2) of 0.9 within a large parameter space. Additionally, a support vector regression (SVR) model obtaining information from Fourier images is proposed for the extraction too, which reaches R^2 of 0.8.

II. METHODS

A. Spin Hamiltonian and micromagnetic simulation

To obtain spin textures with different magnetic Hamiltonian parameters, we use the following spin Hamiltonian:

$$H = -\sum_{\langle i,j \rangle} J_{ij} (\vec{S}_i \cdot \vec{S}_j) - \sum_{\langle i,j \rangle} \vec{d}_{ij} \cdot (\vec{S}_i \times \vec{S}_j)$$
$$- \sum_i K(S_i^z)^2 - \sum_i \mu B S_i^z. \tag{1}$$

Here, J_{ij} and $\vec{d}_{ij}$ represent the Heisenberg exchange coefficient and DMI vector between spin $\vec{S}_i$ and $\vec{S}_j$, respectively. The third summation expression includes single ion anisotropy, which is represented by K, and S_i^z represents the z component of $\vec{S}_i$. Finally, B denotes the z-oriented magnetic field while μ is the magnetic moment of the magnetic atom.

In our simulations, we take into account only the nearest-neighbor interactions. The isotropic exchange interaction is positive, which corresponds to the ferromagnetic case. The DMI has an in-plane orientation and is perpendicular to the corresponding intersite radius vector. The MS [54,55] is performed by the Spirit package [56] with the Landau-Lifshitz-Gilbert equation [57,58]. To avoid the nonuniversal effects of boundary conditions, we use a supercell on the 200×200 square lattice containing 40 000 sites with periodic boundary conditions. To obtain the datasets for training and validating the ML

algorithms, we produce spin textures for the nine different phases which contain classical spin structures and unusual mixed phases. We use the model Hamiltonian presented in Eq. (1), and we take different values in the following ranges: J from 0.1 to 10 meV, D from 0.1 to 2.0 meV, K from 0.1 to 1.0 meV, magnetic field intensity B from 0 to 1.8 T, and temperature T from 0 to 10 K.

B. Texture classification via DNN

As shown in Fig. 1(a), by using the Hamiltonian model presented in Eq. (1) and MS, we produce datasets of spin textures for nine different spin phases [(0) parallel stripes, (1) connected labyrinth, (2) labyrinths and skyrmion, (3) skyrmion gas, (4) fragmented ("wormlike") labyrinth domains and skyrmion, (5) skyrmion lattice, (6) ferromagnetic, (7) domain, and (8) fluctuation], which contain classical spin configurations and unusual mixed phases. These noncollinear magnetic configurations obtained from Spirit simulations describing a 2D ferromagnet are projected on the z axis, which has the advantage of reducing the dataset by a factor of 3 [46,53]. Detecting skyrmion excitation can be achieved through the analysis of only the z components of spins, and such an approach is equally effective in the scenarios of spin spirals, ferromagnetic phases, and some mixed phases. Figure 1(a) also includes diagrams of the spectrum of each phase state, which analyzes the difference among each phase from the perspective of Fourier space. To ensure the adequacy and reliability of the datasets, we have simulated a total of approximately 6000 spin texture images with different configurations.

Then we employ a standard deep neural network architecture containing the fine-tuned Inception-v3 model based on transfer learning for texture classification. Figure 1(b) presents an overview of our transfer learning experiment. The z-projected spin configurations belonging to different phases on the square lattice are considered as input data for the network, which is discussed in detail in Fig. S4 in the Supplemental Material [59]. After training the model with these configurations, the output layer of the network is able to provide the recognized phases corresponding to the input images. For data preprocessing, since the Inception-v3 model is based on a CNN that is a supervised learning algorithm requiring labeled data, as shown in Fig. S1 in the Supplemental Material [59], we propose an automated labeling framework to divide the original images into several different categories.

The whole workflow of data preprocessing is shown in Fig. 1(c). We apply unsupervised learning algorithms such as K-means and hierarchical clustering (for details see Fig. S3 in the Supplemental Material [59]) for the initial division of categories. Specifically, we apply object detection algorithm DETR (for details see Fig. S5 in the Supplemental Material [59]) [60] to identify phases

containing skyrmions. Our approach streamlines the detection pipeline, effectively reducing the requirement for complex manual interventions. After data preprocessing, we may get almost accurate phases which can be trained in deep neural networks to achieve better performance of classification. Additionally, we employ data augmentation techniques to enhance the robustness and generalization of our model, ensuring that the phase category and Hamiltonian parameters remain unaffected by rotation or flipping of the simulated and experimental images, thereby achieving rotation invariance in our model (as shown in Table S2 in the Supplemental Material [59]).

C. Parameter extraction via MISO and SVR

Besides classifying different magnetic phases, we attempt to extract the physical microscopic parameters from spin texture images by ML, which may also be framed as active design of magnetic materials given the spin texture. Two ML architectures are applied for magnetic parameter extraction. The first one, defined as MISO model, is shown at the top of Fig. 2(a), which contains a CNN for images and a multilayer perceptron (MLP) for parameter labels. As shown in Fig. 2(b), it uses the spin texture images and the J, D, and K features of the images mentioned in Sec. II B as the multi-input variables, and aims to estimate the magnetic parameters. This method allows us to accurately extract three key magnetic parameters (J, D, and K) from the input of simulated images and other fixed parameters. Numerous studies have sought efficient approaches for parameter estimation [30,61], but the details regarding the interaction-induced magnetic skyrmionic textures are either incomplete or missing across a huge range of magnetic parameters J, D, and K, and the intricacies of the experimental procedures often make it challenging to precisely capture them [62–64]. While micromagnetic simulations do yield valuable insights [65,66], there may be experimental instances where certain parameters may be challenging to obtain, which is exactly the scenario where MISO is applicable.

The second one is an SVR model [shown at the bottom of Fig. 2(a)] using Fourier-space images as input data and estimating the magnetic parameters. In order to extract features of the spin images to a greater extent, we take the Fourier transform of the original images and perform image scaling, then apply principal components analysis (PCA) to reduce the dimensionality of the data and generate eigenfaces for SVR regression as displayed in Fig. 2(c). Such data preprocessing has been well applied in research on predicting DMI based on images [67], and details are shown in Figs. S18–S21 in the Supplemental Material[59]. These two methods mentioned above are used to extract magnetic parameters from different perspectives and processing modes.
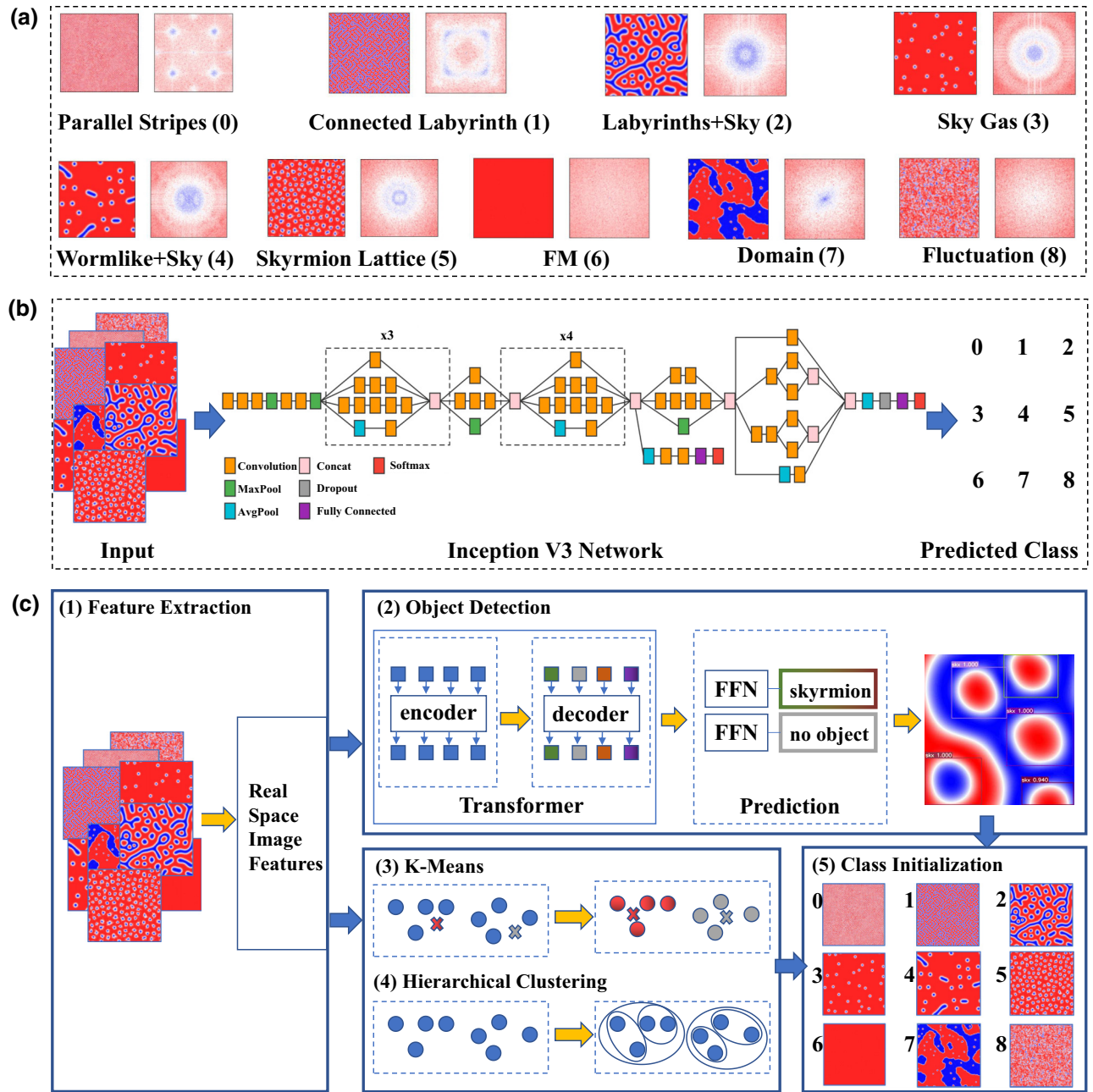
FIG. 1.   (a) The spin textures of nine phases obtained from micromagnetic simulation and their spectra. (b) The architecture of the neural network used for phase classification. Simulated spin textures act as input data, entering the whole network and then match the corresponding classes. (c) Data preprocessing operation for automatically labeling and initializing dataset (shown as (5)) before training the deep learning model, including (1) feature extraction, (2) object detection algorithm, and unsupervised learning methods such as (3) K-means and (4) hierarchical clustering.

III. RESULTS AND DISCUSSION

The magnetic behavior governed by the model presented in Eq. (1) is influenced by the magnetic Hamiltonian parameters, magnetic field, and temperature. Based on such a model, micromagnetic simulations allow us to obtain massive spin texture images for different configurations. As these simulations produce more variations and complex phases, we attempt to simply identify the amount of skyrmions and classify skyrmionic textures. Here we discuss the implementation of the object detection algorithm to realize the recognition of skyrmions in detail.

Figure 3(a) gives the mean average precision (mAP; COCO style) learning curve of DETR (COCO is the "Common Objects in Context" dataset), which is trained
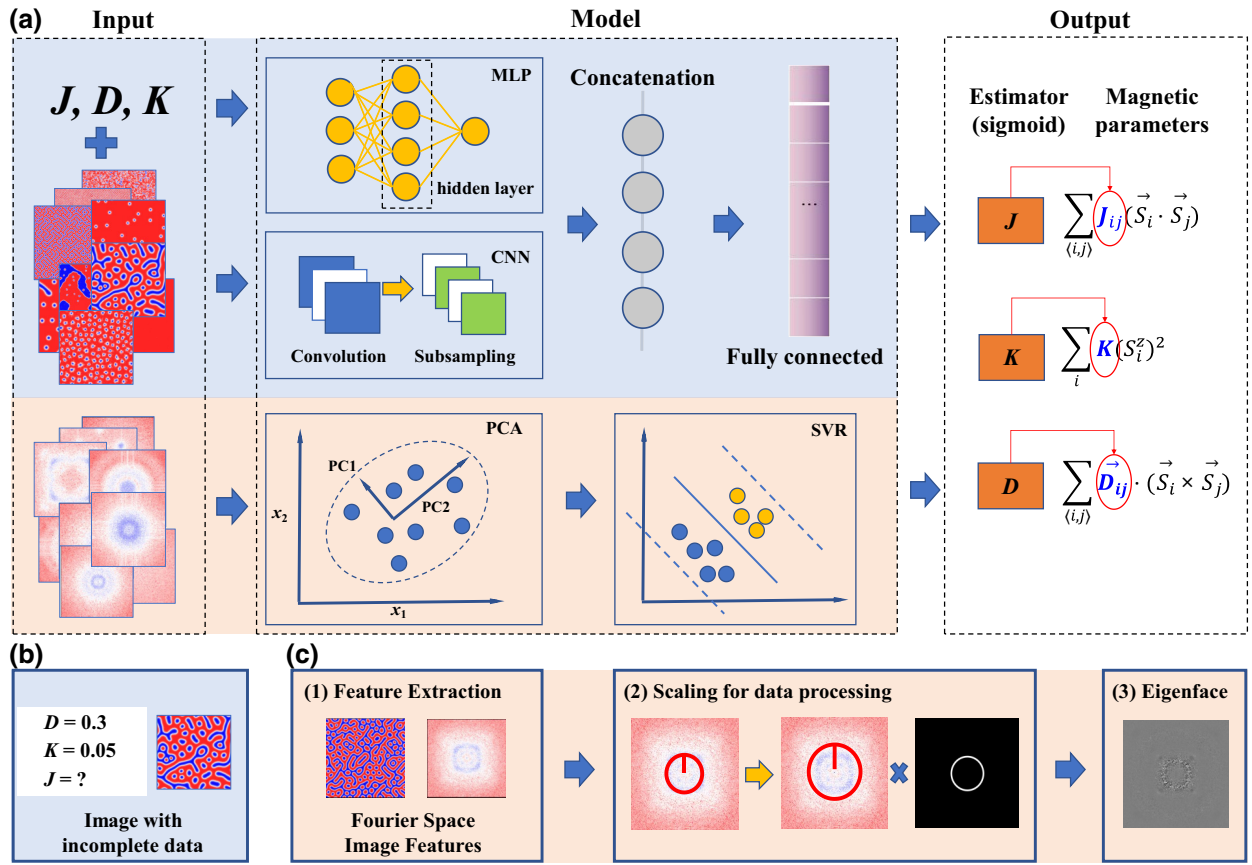
FIG. 2. The architecture of the machine learning methods used for parameter determination. (a) The top part (pale blue background) shows the MISO deep learning model, which combines information from two subnetworks to detect the parameters. It takes two inputs: image features and numerical parameter features, which are learned separately using subnetworks (CNN for images, and MLP for numerical value). The bottom part (pale orange background) shows the SVR, which uses Fourier-space features of images as input and outputs the estimated values of parameters. (b) The input data contain image data and the incomplete numerical parameter data for the MISO model. (c) Data pretreatment for the SVR regression model including (1) feature extraction from real space to Fourier space, and (2) scaling images to filter out effective areas. (3) After such preprocessing, eigenfaces that contain the most information of a single image are synthesized.

end-to-end with a set loss function (shown as Eq. (S1) in the Supplemental Material [59]) and performs bipartite matching between predicted and ground-truth objects. To train the model, we label skyrmion as the target to be identified based on the image datasets of Fig. 1(a), and reason about the relations of the skyrmions and the global image context to directly output the final set of predictions in parallel. We can see that the detected skyrmions are accurately located and plotted in the inset map of Fig. 3(a). When the learning rate decreases, DETR significantly boosts the recognition performance, with a large mAP, which indicates that this object detection model has achieved high accuracy.

Generally, different spin phases can be simply identified and distinguished by the number of skyrmions. After using DETR to recognize skyrmions accurately, we simultaneously investigate the evolution of spin phases with a different ratio between DMI and Heisenberg exchange

interaction (D/J), and take into account the influence of magnetic field (M) and temperature (T). Considering the influence of temperature, when D/J ranges from 0.1 to 0.5, as shown in Fig. 3(b), the temperature takes the system from a stable phase containing skyrmions to a phase of thermal fluctuation (from mixed state 2 to state 8), which implies that, the higher the temperature, the stronger the spin thermal fluctuation and the more unstable the skyrmion state. When D/J falls inside the typical range around 0.2 for the formation of skyrmions, the skyrmions can be obtained at a relatively low temperature, which is consistent with the previous report [68].

As shown in Fig. 3(c), when the magnetic field increases, the system changes from a spiral phase (Sp, state 1) induced at zero field to a skyrmion crystal (SkX, state 5), and then to a ferromagnetic (FM, state 6) state at higher M for a small value of D/J. At a larger D/J, the magnetic field brings the system from a mixed phase
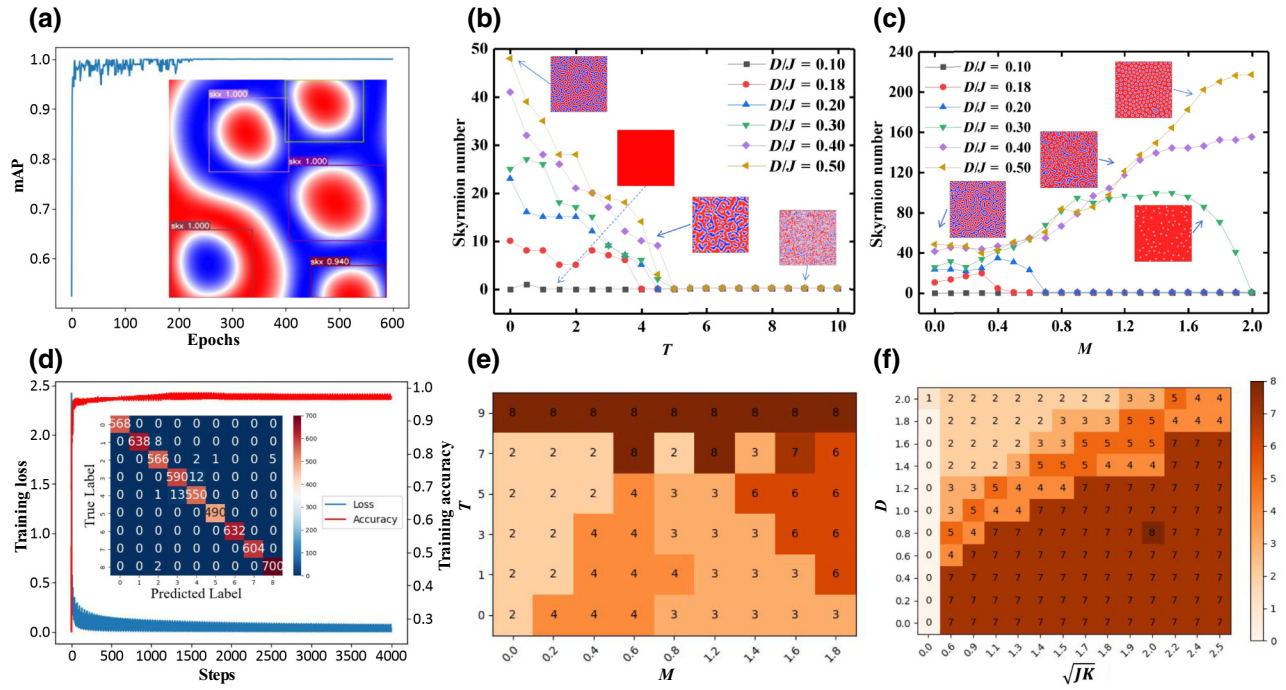
FIG. 3. Training result and recognition result of ML methods used for phase classification. (a) The learning curves of mean average precision for DETR with the model trained for 300 epochs. The inset is the detection result of a texture containing five skyrmions. (b) The skyrmion number as a function of temperature T (K) when M is set as 0.2 T. (c) The skyrmion number as a function of magnetic field M (T) when T is set as 0 K. (d) The trends in loss and accuracy of the DNN model as the number of training steps increases. The inset shows the confusion matrix. (e) The M (T) vs. T (K) phase diagram at $D/J = 0.3$ with $K = 0.25$ meV. (f) The $\sqrt{JK}$ (meV) vs. D (meV) phase diagram at $M = 0.6$ T.

containing skyrmions and labyrinths to a skyrmion crystal. These intermediate phases are enhanced by temperature and should disappear in the zero-temperature limit. When D/J is relatively small, the exchange interaction plays a dominant role, which reduces the vortices in the FM background and causes the rotation of the magnetic moments from the $-z$ direction at the center of the skyrmion to the z direction at the boundary at a small atomic scale. In this case, skyrmions with relatively small size and low density can be obtained. Upon decreasing D/J close to zero, DMI is negligible, and the strong magnetic exchange coupling J leads to the parallel arrangement of the magnetic moments, that is, the FM phase. On the other hand, when D/J is large enough, DMI plays a dominant role, benefiting the emergence of labyrinth domains.

As in the analysis above, we have discussed in detail the derivation of skyrmionic textures under the influence of Hamiltonian parameters, magnetic field, and temperature. By using nine spin phases generated under different parameters, magnetic fields, and temperature, we train the standard DNN model for texture classification. The training accuracy and loss of this deep learning framework is shown in Fig. 3(d). The inset shows that all the test data are presented on the diagonal of the confusion matrix

which describes the effectiveness of the classification for the test dataset, with predicted label as x axis and true label as y axis. The details of model performance are shown in Figs. S7 and S8 in the Supplemental Material [59]. The results of our experiments unequivocally demonstrate the superior performance of our model compared to existing benchmarks. Tables S4 and S5 in the Supplemental Material [59] outline the key metrics, showcasing an improvement in accuracy and applicability over other models.

Detailed phase diagrams taking into account the magnetic field (M) and temperature (T) as well as the ratio of the magnetic parameters can be seen in the following steps. As we can see in Fig. 3(e), when the parameters are set as $D/J = 0.3$ and $K = 0.25$ meV, the phases containing skyrmions (states 2, 3, and 4) occupy the majority of the M-T phase diagram. As the magnetic field increases, the system changes from the mixed phase of labyrinths and skyrmions (state 2) to that of wormlike and skyrmion (state 4), skyrmion gas (state 3), and ferromagnetic (state 5) phase which then appear at higher T, which indicates that magnetic field influences the stability of skyrmions. At the same time, the change in temperature affects the appearance of the entire phase diagram from the perspective of thermal stability.

Based on this deep learning model, we also investigate the formation conditions of the skyrmion lattice. As we have established the roles of D and J, we next take into account the effect of K on the topological spin textures. As shown in Fig. 3(f), intriguingly, the relationship between D and $\sqrt{JK}$ of the skyrmion lattice phase, which is referred to as state 5, is linear under magnetic fields of 0.6 T (corresponding to the authoritative report [69]). This suggests that $D/\sqrt{JK}$ can be used to estimate the formation of the skyrmion lattice, and further can be a judgment condition of the materials' properties.

As mentioned above, the D, J, and K values can significantly affect the formation and characteristics of different skyrmionic textures. Next, we attempt to identify a universal descriptor based on these three Hamiltonian magnetic

parameters. As shown in Fig. 4, the values of J, D, and K can largely determine a certain spin phase while adopting the control variate method, that is, each group of phase diagrams only studies one variable. As demonstrated in Fig. 4(a), we can see that J largely determines the skyrmion magnetic textures within the same regulatory regions of D and K, where D (K) ranged from 0.0 to 2.0 (1.0) meV. When D increases, the parallel stripes phase (state 0) or the connected labyrinth phase (state 1) begins to appear and expand at a low value of J. Then, the disconnected labyrinths (state 2) and skyrmion gas (state 3) appears with higher J. The larger J tends to break the disconnected labyrinth domain into fragmental domains mixed with skyrmions. In addition, when K increases, the domain phase (state 7) is gradually dominant. With
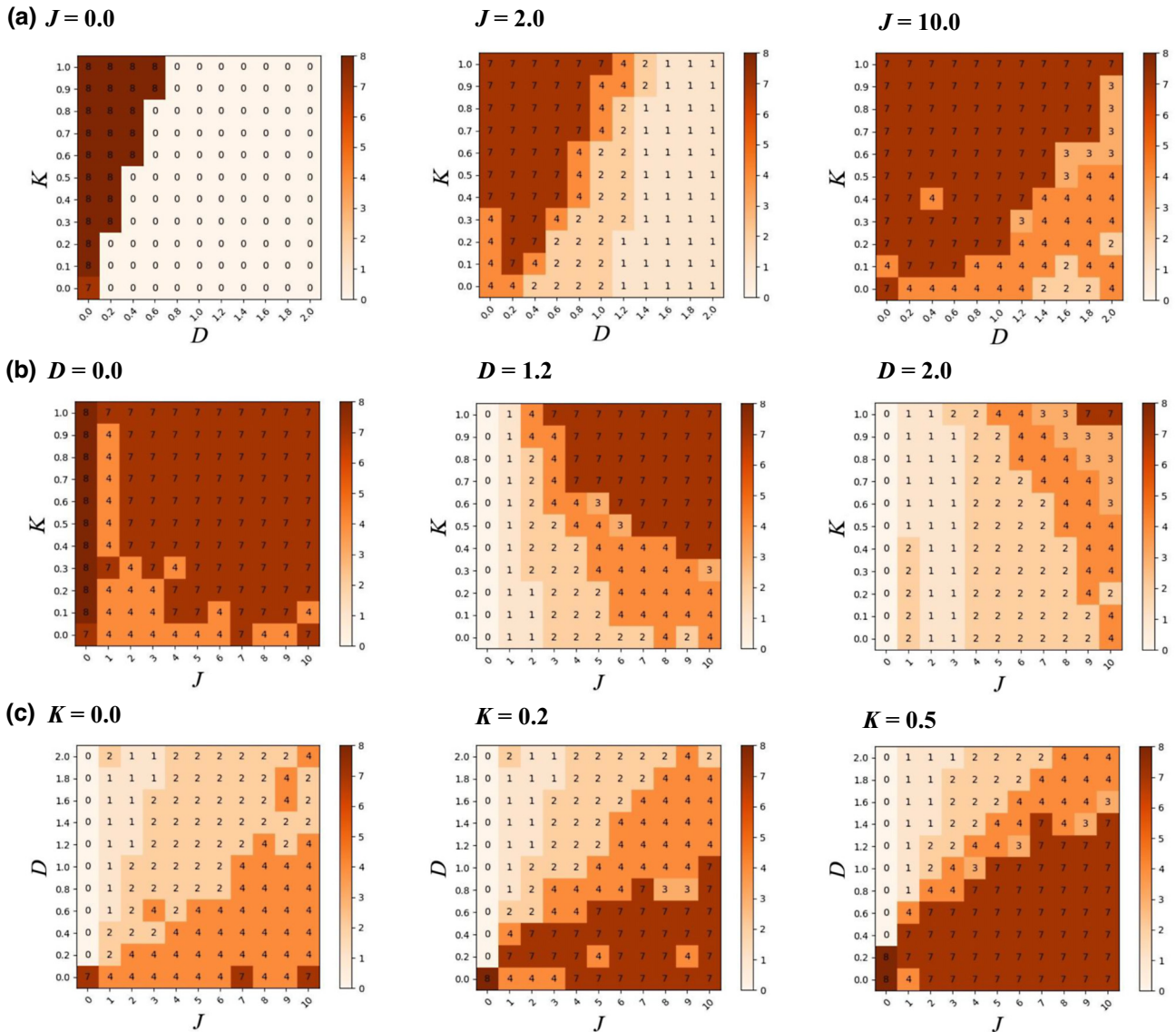

FIG. 4. The phase diagrams of (a) K-D, (b) K-J, and (c) D-J are shown when (a) J is set at 0, 2, and 10 meV, (b) D is set at 0.0, 1.2, and 2.0 meV, and (c) K is set at 0.0, 0.2, and 0.5 meV, respectively.

increases in J, the distribution area of domains (state 7) becomes greater, and overall each mixed phase extends along the diagonal direction substantially.

Similarly, when it comes to Fig. 4(b), with the increase of D, the parallel stripes phase (state 1) and the phase with few skyrmions (states 2 to 4) begin to expand. At the same time, the domain phase (state 7) will be squeezed along the diagonal direction. Furthermore, if D attains a larger value, the spin texture contains the states of labyrinth domains (state 2) and parallel stripes (state 0) in a larger parameter space of J and K. What can be concluded is that the increase of D leads to the density of labyrinth domains (state 2) to increase. What is more, with J increasing, the fluctuation phases (state 8) may gradually dominate, and with D increases, the distribution area of domain phases (state 7) becomes less and comes with the appearance of skyrmion gas (state 3).

After studying the phase distribution in phase diagrams under the influence of both J and D, the impact of K also follows the above patterns, which is shown in Fig. 4(c). As K increases, the phases related to labyrinth domains (state 2) and skyrmions (state 4) occupy less area in the phase diagram. This can be understood according to the following description: When K is positive, the energy gain provided by the perpendicular magnetic anisotropy begins to sustain an out-of-plane spin alignment, thereby promoting the formation of Néel-type skyrmions. In addition, similar to J, K tends to force the magnetic moment into a parallel arrangement. In this regard, a large $|K|$ can suppress the modulation of labyrinth domains and skyrmions.

In addition, we have incorporated experimental images [70–75] into our testing datasets, addressing the necessity of evaluating our models. Our models continue to showcase strong performance, capturing the nuances present in experimental samples and reaffirming the validity of our approach, as shown in Fig. S9 in the Supplemental Material [59].

We now come to the ML models for the extraction of Hamiltonian magnetic parameters. For a clear illustration, we show only the results of simulated images belonging to the chiral ferromagnetic system ($J > 0$). Figure 5(a) shows a set of simulated spin configurations using a series of magnetic parameters J, D, and K as the training and testing datasets. These images of spin textures and their magnetic parameters of J, D, and K are input into the MISO deep learning network mentioned in the top row of Fig. 2(a), and the performance of the model is shown in Fig. 5(b), which shows the low loss and high R^2 meet good standards.

Meanwhile, we perform a Fourier transform on all the images in the parameter space to obtain image features. Inputting the eigenfaces generated from the Fourier images
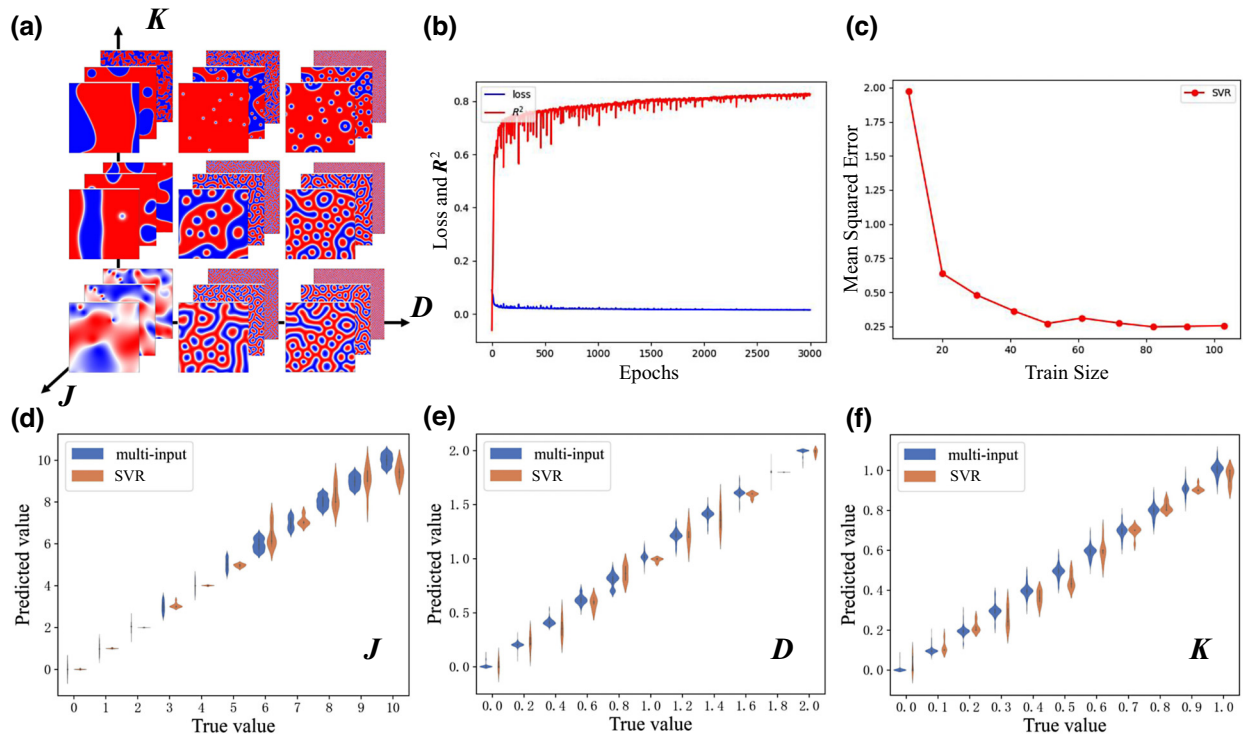

FIG. 5. Regression prediction of Hamiltonian magnetic parameters tested on simulation images. (a) Spin configurations generated by MS with the parameter spaces of J, D, and K used in the training data. (b) The loss and R^2 for the parameter extraction of the MISO model. (c) The learning curve of the SVR model. (d)–(f) Plots of the estimated values as a function of the true values for J, D, and K, respectively.

via PCA into the SVR model introduced in the bottom row of Fig. 2(a), we can get the same predicted sets of magnetic parameters J, D, and K. Figure 5(c) gives the learning curve of the SVR model, while the mean squared error (MSE) follows the formula: $\mathrm{MSE}(y, y') = \left(\sum_{i=1}^{n}(y_i - y_i')^2\right)/n$. Here, n is the number of samples, y_i is the true value of the ith sample, and y_i' is the predicted value of the model for the ith sample. The learning curve shows that, as the training size increases, the difference between the predicted and true values of the model decreases.

In addition to proving the accuracy of the model through loss, accuracy, and MSE curves, the matching results of the predicted values and true parameters can also prove the reliability of the model. The estimated values of J, D, and K were plotted in Figs. 5(d)–5(f), where the violin plots indicate the deviation between predicted results and the true values of the parameters. The values estimated by the MISO model are marked in blue, while those estimated by the SVR model are marked in orange. It can be seen that there exist few errors for the extraction of these parameters through the two models. For example, the extraction of J is fairly good when J is not so large, and deviations of D are slightly larger when it is in the middle range but still within an acceptable level. The predicted values and the true values follow a linear curve, indicating the general ability for extraction on all samples with different parameter sets. For comparison, the MISO model has higher accuracy in predicting J and D, but is slightly inferior to the SVR model in the process of predicting K.

IV. CONCLUSIONS

This paper employs ML methods and MS to categorize skyrmionic textures and extract magnetic Hamiltonian parameters within the 2D Heisenberg model, incorporating Heisenberg exchange interaction (J), Dzyaloshinskii-Moriya interaction (D), and single-ion anisotropy (K). Utilizing MS image results, we generate a substantial dataset comprising 6000 spin textures, and propose an automated labeling framework to divide the original images into nine different categories via K-means and hierarchical clustering. The DNN model based on Inception-V3 architecture exhibits high accuracy in classifying skyrmionic textures and discerning phase boundaries between the mixed phases. We recognize skyrmions accurately and simultaneously study the influence of magnetic field and temperature on phase transitions with the cutting-edge algorithm DETR.

Subsequently, precise phase diagrams are obtained under the manipulation of the temperature, magnetic field, and magnetic Hamiltonian parameters J, D, and K, demonstrating remarkable agreement when compared with simulation results. The MISO model handling both images and parameters and the SVR model obtaining information from

Fourier images have achieved high R^2 of 0.90 (MISO) and 0.8 (SVR) for the extraction of Hamiltonian magnetic parameters.

The precise models presented in our work offer theoretical support for classifying experimentally obtained skyrmionic textures and underscore the feasibility of extracting microscopic mechanisms of Hamiltonian parameters from skyrmionic images.

[1] K. S. Burch, D. Mandrus, and J. G. Park, Magnetism in two-dimensional van der Waals materials, Nature **563,** 47 (2018).

[2] S. D. Bader, Colloquium: Opportunities in nanomagnetism, Rev. Mod. Phys. **78,** 1 (2006).

[3] D. P. Pappas, K.-P. Kämper, and H. Hopster, Reversible Transition Between Perpendicular and In-Plane Magnetization in Ultrathin Films, Phys. Rev. Lett. **64,** 3179 (1990).

[4] R. Allenspach and A. Bischof, Magnetization Direction Switching in Fe/Cu(100) Epitaxial Films: Temperature and Thickness Dependence, Phys. Rev. Lett. **69,** 3385 (1992).

[5] R. Ramchal, A. K. Schmid, M. Farle, and H. Poppa, Spiral-like continuous spin-reorientation transition of Fe/Ni bilayers on Cu(100), Phys. Rev. B **69,** 214401 (2004).

[6] C. Won, Y. Z. Wu, J. Choi, W. Kim, A. Scholl, A. Doran, T. Owens, J. Wu, X. F. Jin, and Z. Q. Qiu, Magnetic stripe melting at the spin reorientation transition in Fe/Ni/Cu(001), Phys. Rev. B **71,** 224429 (2005).

[7] Z. Q. Qiu, J. Pearson, and S. D. Bader, Asymmetry of the Spin Reorientation Transition in Ultrathin Fe Films and Wedges Grown on Ag(100), Phys. Rev. Lett. **70,** 1006 (1993).

[8] S. T. Chui and V. N. Ryzhov, Soliton and 2D Domains in Ultrathin Magnetic Films, Phys. Rev. Lett. **78,** 2224 (1997).

[9] E. Y. Vedmedenko, A. Ghazali, and J.-C. S. Lévy, Magnetic vortices in ultrathin films, Phys. Rev. B **59,** 3329 (1999).

[10] E. Vedmedenko, A. Ghazali, and J.-C. Lévy, Magnetic structures of Ising and vector spins monolayers by Monte-Carlo simulations, Surf. Sci. **402-404,** 391 (1998).

[11] S. S. Parkin, M. Hayashi, and L. Thomas, Magnetic domain-wall racetrack memory, Science **320,** 190 (2008).

[12] S. Muhlbauer, B. Binz, F. Jonietz, C. Pfleiderer, A. Rosch, A. Neubauer, R. Georgii, and P. Boni, Skyrmion lattice in a chiral magnet, Science **323,** 915 (2009).

[13] N. Nagaosa and Y. Tokura, Topological properties and dynamics of magnetic skyrmions, Nat. Nanotechnol. **8,** 899 (2013).

[14] D. A. Gilbert, B. B. Maranville, A. L. Balk, B. J. Kirby, P. Fischer, D. T. Pierce, J. Unguris, J. A. Borchers, and K.

Liu, Realization of ground-state artificial skyrmion lattices at room temperature, Nat. Commun. **6**, 8462 (2015).

[15] A. O. Leonov, C. Pappas, and I. I. Smalyukh, Field-driven metamorphoses of isolated skyrmions within the conical state of cubic helimagnets, Phys. Rev. B **104**, 064432 (2021).

[16] Y. Wang, Y. Feng, Y. Zhu, Y. Tang, L. Yang, M. Zou, W. Geng, M. Han, X. Guo, B. Wu, and X. L. Ma, Polar meron lattice in strained oxide ferroelectrics, Nat. Mater. **19**, 881 (2020).

[17] A. R. Damodaran, J. Clarkson, Z. Hong, H. Liu, A. K. Yadav, C. T. Nelson, S.-L. Hsu, M. McCarter, K.-D. Park, V. Kravtsov *et al.*, Phase coexistence and electric-field control of toroidal order in oxide superlattices, Nat. Mater. **16**, 1003 (2017).

[18] S. Bera and S. S. Mandal, Theory of the skyrmion, meron, antiskyrmion, and antimeron in chiral magnets, Phys. Rev. Res. **1**, 033109 (2019).

[19] J. Puebla, J. Kim, K. Kondou, and Y. Otani, Spintronic devices for energy-efficient data storage and energy harvesting, Commun. Mater. **1**, 24 (2020).

[20] K. Karube, J. S. White, D. Morikawa, C. D. Dewhurst, R. Cubitt, A. Kikkawa, X. Yu, Y. Tokunaga, T. hisa Arima, H. M. Rønnow, Y. Tokura, and Y. Taguchi, Disordered skyrmion phase stabilized by magnetic frustration in a chiral magnet, Sci. Adv. **4**, eaar7043 (2018).

[21] T. Tanigaki, K. Shibata, N. Kanazawa, X. Yu, Y. Onose, H. S. Park, D. Shindo, and Y. Tokura, Real-space observation of short-period cubic lattice of skyrmions in MnGe, Nano Lett. **15**, 5438 (2015).

[22] X. Yu, N. Kanazawa, Y. Onose, K. Kimoto, W. Zhang, S. Ishiwata, Y. Matsui, and Y. Tokura, Near room-temperature formation of a skyrmion crystal in thin-films of the helimagnet FeGe, Nat. Mater. **10**, 106 (2011).

[23] D. Feng, Z. Shen, Y. Xue, Z. Guan, R. Xiao, and C. Song, Strain-induced magnetic phase transition, magnetic anisotropy switching and bilayer antiferromagnetic skyrmions in van der Waals magnet CrTe$_2$, Nanoscale **15**, 1561 (2023).

[24] Z. Shen, Y. Xue, Z. Wu, and C. Song, Enhanced Curie temperature and skyrmion stability by strain in room temperature ferromagnetic semiconductor CrISe monolayer, Appl. Phys. Lett. **121**, 202402 (2022).

[25] Z. Shen, C. Song, Y. Xue, Z. Wu, J. Wang, and Z. Zhong, Strain-tunable Dzyaloshinskii-Moriya interaction and skyrmions in two-dimensional Janus Cr$_2X_3Y_3$ (X, Y = Cl, Br, I, $X \neq Y$) trihalide monolayers, Phys. Rev. B **106**, 094403 (2022).

[26] I. D., A thermodynamic theory of "weak" ferromagnetism of antiferromagnetics, J. Phys. Chem. Solids **4**, 241 (1958).

[27] T. Moriya, Anisotropic superexchange interaction and weak ferromagnetism, Phys. Rev. **120**, 91 (1960).

[28] N. Cartwright and E. McMullin, How the laws of physics lie, Am. J. Phys. **52**, 474 (1984).

[29] W. F. Brown Jr, Some magnetostatic and micromagnetic properties of the infinite rectangular bar, J. Appl. Phys. **35**, 2102 (1964).

[30] D. Wang, S. Wei, A. Yuan, F. Tian, K. Cao, Q. Zhao, Y. Zhang, C. Zhou, X. Song, D. Xue *et al.*, Machine learning magnetic parameters from spin configurations, Adv. Sci. **7**, 2000566 (2020).

[31] J. Leliaert, M. Dvornik, J. Mulkers, J. D. Clercq, M. V. Milošević, and B. V. Waeyenberge, Fast micromagnetic simulations on GPU – Recent advances made with mumax^3, J. Phys. D: Appl. Phys. **51**, 123002 (2018).

[32] L. Passell, O. W. Dietrich, and J. Als-Nielsen, Neutron scattering from the Heisenberg ferromagnets EuO and EuS. I. The exchange interactions, Phys. Rev. B **14**, 4897 (1976).

[33] G. Shirane, V. Minkiewicz, and R. Nathans, Spin waves in 3D metals, J. Appl. Phys. **39**, 383 (1968).

[34] S. P. Vernon, S. M. Lindsay, and M. B. Stearns, Brillouin scattering from thermal magnons in a thin Co film, Phys. Rev. B **29**, 4439 (1984).

[35] C. Eyrich, W. Huttema, M. Arora, E. Montoya, F. Rashidi, C. Burrowes, B. Kardasz, E. Girt, B. Heinrich, O. Mryasov *et al.*, Exchange stiffness in thin film Co alloys, J. Appl. Phys. **111**, 07C919 (2012).

[36] X. Liu, M. M. Steiner, R. Sooryakumar, G. A. Prinz, R. F. C. Farrow, and G. Harp, Exchange stiffness, magnetization, and spin waves in cubic and hexagonal phases of cobalt, Phys. Rev. B **53**, 12166 (1996).

[37] S. Klingler, A. V. Chumak, T. Mewes, B. Khodadadi, C. Mewes, C. Dubs, O. Surzhenko, B. Hillebrands, and A. Conca, Measurements of the exchange stiffness of YIG films using broadband ferromagnetic resonance techniques, J. Phys. D: Appl. Phys. **48**, 015001 (2014).

[38] D. Burgarth and A. Ajoy, Evolution-Free Hamiltonian Parameter Estimation through Zeeman Markers, Phys. Rev. Lett. **119**, 030402 (2017).

[39] J. Zhang and M. Sarovar, Quantum Hamiltonian Identification from Measurement Time Traces, Phys. Rev. Lett. **113**, 080401 (2014).

[40] B. Buford, P. Dhagat, and A. Jander, Estimating exchange stiffness of thin films with perpendicular anisotropy using magnetic domain images, IEEE Magn. Lett. **7**, 1 (2016).

[41] G. Carleo and M. Troyer, Solving the quantum many-body problem with artificial neural networks, Science **355**, 602 (2017).

[42] B. S. Rem, N. Käming, M. Tarnowski, L. Asteria, N. Fläschner, C. Becker, K. Sengstock, and C. Weitenberg, Identifying quantum phase transitions using artificial neural networks on experimental data, Nat. Phys. **15**, 917 (2019).

[43] L. Wang, Discovering phase transitions with unsupervised learning, Phys. Rev. B **94**, 195105 (2016).

[44] E. P. Van Nieuwenburg, Y.-H. Liu, and S. D. Huber, Learning phase transitions by confusion, Nat. Phys. **13**, 435 (2017).

[45] J. Carrasquilla and R. G. Melko, Machine learning phases of matter, Nat. Phys. **13**, 431 (2017).

[46] I. A. Iakovlev, O. M. Sotnikov, and V. V. Mazurenko, Supervised learning approach for recognizing magnetic skyrmion phases, Phys. Rev. B **98**, 174411 (2018).

[47] D. Liu, Z. Liu, J. Zhang, Y. Yin, J. Xi, L. Wang, J. Xiong, M. Zhang, T. Zhao, J. Jin, F. Hu, J. Sun, J. Shen, and B. Shen, Classification and prediction of skyrmion material based on machine learning, Research **6**, 0082 (2023).

[48] W. Wang, Z. Wang, Y. Zhang, B. Sun, and K. Xia, Learning order parameters from videos of skyrmion dynamical phases with neural networks, Phys. Rev. Appl. **16**, 014005 (2021).

[49] J. Salcedo-Gallo, C. Galindo-González, and E. Restrepo-Parra, Deep learning approach for image classification of

magnetic phases in chiral magnets, J. Magn. Magn. Mater. **501,** 166482 (2020).

[50] V. K. Singh and J. H. Han, Application of machine learning to two-dimensional Dzyaloshinskii-Moriya ferromagnets, Phys. Rev. B **99,** 174426 (2019).

[51] T. Matthies, A. F. Schäffer, T. Posske, R. Wiesendanger, and E. Y. Vedmedenko, Topological characterization of dynamic chiral magnetic textures using machine learning, Phys. Rev. Appl. **17,** 054022 (2022).

[52] T. Kawaguchi, K. Takagi, and N. Takagi, Rapid single-flux-quantum logic circuits using clockless gates, IEEE Trans. Appl. Supercond. **31,** 1 (2021).

[53] F. A. Gómez Albarracín and H. D. Rosales, Machine learning techniques to construct detailed phase diagrams for skyrmion systems, Phys. Rev. B **105,** 214423 (2022).

[54] M. Hoffmann, B. Zimmermann, G. P. Muller, D. Schurhoff, N. S. Kiselev, C. Melcher, and S. Blugel, Antiskyrmions stabilized at interfaces by anisotropic Dzyaloshinskii-Moriya interactions, Nat. Commun. **8,** 308 (2017).

[55] S. Hayami, In-plane magnetic field-induced skyrmion crystal in frustrated magnets with easy-plane anisotropy, Phys. Rev. B **103,** 224418 (2021).

[56] G. P. Müller, M. Hoffmann, C. Dißelkamp, D. Schürhoff, S. Mavros, M. Sallermann, N. S. Kiselev, H. Jónsson, and S. Blügel, Spirit: Multifunctional framework for atomistic spin simulations, Phys. Rev. B **99,** 224414 (2019).

[57] L. LANDAU and E. LIFSHITZ, On the theory of the dispersion of magnetic permeability in ferromagnetic bodies − Reprinted from Physikalische Zeitschrift der Sowjetunion 8, part 2, 153, 1935, in *Perspectives in Theoretical Physics*, edited by L. Pitaevski (Pergamon, Amsterdam, 1992), p. 51.

[58] T. Gilbert, A phenomenological theory of damping in ferromagnetic materials, IEEE Trans. Magn. **40,** 3443 (2004).

[59] See Supplemental Material http://link.aps.org/supplemental/10.1103/PhysRevApplied.21.034009 for: (1) algorithm description for phase classification and clustering; (2) algorithm description for parameter estimation; (3) detailed phase diagrams under different magnetic parameters; and (4) detailed data process for estimation of magnetic parameters.

[60] N. Carion, F. Massa, G. Synnaeve, N. Usunier, A. Kirillov, and S. Zagoruyko, in *Computer Vision − ECCV 2020*, Vol. 12346 (Springer International Publishing, Cham, 2020), p. 213.

[61] J. F. Kong, Y. Ren, M. S. N. Tey, P. Ho, K. H. Khoo, X. Chen, and A. Soumyanarayanan, Quantifying the magnetic interactions governing chiral spin textures using deep neural networks, ACS Appl. Mater. Inter. **16,** 1025 (2024).

[62] V. Dmitrienko, E. Ovchinnikova, S. Collins, G. Nisbet, G. Beutier, Y. Kvashnin, V. Mazurenko, A. Lichtenstein, and M. Katsnelson, Measuring the Dzyaloshinskii–Moriya interaction in a weak ferromagnet, Nat. Phys. **10,** 202 (2014).

[63] D.-S. Han, N.-H. Kim, J.-S. Kim, Y. Yin, J.-W. Koo, J. Cho, S. Lee, M. Klaui, H. J. Swagten, B. Koopmans *et al.*, Asymmetric hysteresis for probing Dzyaloshinskii–Moriya interaction, Nano Lett. **16,** 4438 (2016).

[64] M. Kuepferling, A. Casiraghi, G. Soares, G. Durin, F. Garcia-Sanchez, L. Chen, C. H. Back, C. H. Marrows, S. Tacchi, and G. Carlotti, Measuring interfacial Dzyaloshinskii-Moriya interaction in ultrathin magnetic films, Rev. Mod. Phys. **95,** 015003 (2023).

[65] M. Altthaler, E. Lysne, E. Roede, L. Prodan, V. Tsurkan, M. A. Kassem, H. Nakamura, S. Krohns, I. Kézsmárki, and D. Meier, Magnetic and geometric control of spin textures in the itinerant kagome magnet Fe_3Sn_2, Phys. Rev. Res. **3,** 043191 (2021).

[66] A. Hallal, J. Liang, F. Ibrahim, H. Yang, A. Fert, and M. Chshiev, Rashba-type Dzyaloshinskii-Moriya interaction, perpendicular magnetic anisotropy, and skyrmion states at 2D materials/Co interfaces, Nano Lett. **21,** 7138 (2021).

[67] P. Agrawal, F. Büttner, I. Lemesh, S. Schlotter, and G. S. D. Beach, Measurement of interfacial Dzyaloshinskii-Moriya interaction from static domain imaging, Phys. Rev. B **100,** 104430 (2019).

[68] A. Fert, V. Cros, and J. Sampaio, Skyrmions on the track, Nat. Nanotechnol. **8,** 152 (2013).

[69] W. Du, K. Dou, Z. He, Y. Dai, B. Huang, and Y. Ma, Spontaneous magnetic skyrmions in single-layer $CrInX_3$ (X = Te, Se), Nano Lett. **22,** 3440 (2022).

[70] X. Yu, Y. Onose, N. Kanazawa, J. H. Park, J. Han, Y. Matsui, N. Nagaosa, and Y. Tokura, Real-space observation of a two-dimensional skyrmion crystal, Nature **465,** 901 (2010).

[71] M. Birch, D. Cortés-Ortuño, L. Turnbull, M. Wilson, F. Groß, N. Träger, A. Laurenson, N. Bukin, S. Moody, M. Weigand *et al.*, Real-space imaging of confined magnetic skyrmion tubes, Nat. Commun. **11,** 1726 (2020).

[72] L. Peng, Y. Zhang, W. Wang, M. He, L. Li, B. Ding, J. Li, Y. Sun, X.-G. Zhang, J. Cai *et al.*, Real-space observation of nonvolatile zero-field biskyrmion lattice generation in MnNiGa magnet, Nano Lett. **17,** 7075 (2017).

[73] X. Yu, F. Kagawa, S. Seki, M. Kubota, J. Masell, F. S. Yasin, K. Nakajima, M. Nakamura, M. Kawasaki, N. Nagaosa *et al.*, Real-space observations of 60-nm skyrmion dynamics in an insulating magnet under low heat flow, Nat. Commun. **12,** 5079 (2021).

[74] J. Zhang, M. Wang, Z. Zhang, H. Huang, L. Zhu, D. Liu, H. Zhang, F. Han, H. Yang *et al.*, Direct observation of magnetic skyrmions and their current-induced dynamics in epitaxial single-crystal oxide films, Nano Lett. **23,** 4258 (2023).

[75] R. Zhu, Z. Jiang, X. Zhang, X. Zhong, C. Tan, M. Liu, Y. Sun, X. Li, R. Qi, K. Qu *et al.*, Dynamics of Polar Skyrmion Bubbles under Electric Fields, Phys. Rev. Lett. **129,** 107601 (2022).